

From Subpixel to Superpixel: A Novel Fusion Framework for Hyperspectral Image Classification

Ting Lu, *Student Member, IEEE*, Shutao Li, *Senior Member, IEEE*, Leyuan Fang, *Member, IEEE*,
Xiuping Jia, *Senior Member, IEEE*, and Jón Atli Benediktsson, *Fellow, IEEE*

Abstract—Supervised classification of hyperspectral images (HSI) is a very challenging task due to the existence of noisy and mixed spectral characteristics. Recently, the widely developed spectral unmixing techniques offer the possibility to extract spectral mixture information at a subpixel level, which can contribute to the categorization of seriously mixed spectral pixels. Besides, it has been demonstrated that the discrimination between different materials will be improved by integrating the geometry and structure information, which can be derived from the variance between neighboring pixels. Furthermore, by incorporating the spatial context, the superpixel-based spectral–spatial similarity information can be used to smooth classification results in homogeneous regions. Therefore, a novel fusion framework for HSI classification that combines subpixel, pixel, and superpixel-based complementary information is proposed in this paper. Here, both feature fusion and decision fusion schemes are introduced. For the feature fusion scheme, the first step is to extract subpixel-level, pixel-level, and superpixel-level features from HSI, respectively. Then, the multiple feature-induced kernels are fused to form one composite kernel, which is incorporated with a support vector machine (SVM) classifier for label assignment. For the decision fusion scheme, class probabilities based on three different features are estimated by the probabilistic SVM classifier first. Then, the class probabilities are adaptively fused to form a probabilistic decision rule for classification. Experimental results tested on different real HSI images can demonstrate the effectiveness of the proposed fusion schemes in improving discrimination capability, when compared with the classification results relied on each individual feature.

Index Terms—Decision fusion, feature fusion, hyperspectral image (HSI) classification, pixel, subpixel, superpixel.

I. INTRODUCTION

HYPERSPECTRAL sensors are now able to collect hundreds of spectral bands, corresponding to a wide range

Manuscript received November 16, 2016; revised March 9, 2017; accepted April 4, 2017. This paper was supported in part by the National Natural Science Fund of China for Distinguished Young Scholars under Grant 61325007 and in part by the National Natural Science Fund of China for International Cooperation and Exchanges under Grant 61520106001. (*Corresponding author: Shutao Li*)

T. Lu, S. Li, and L. Fang are with the College of Electrical and Information Engineering, Hunan University, Changsha 410082, China (e-mail: tingluhnu@gmail.com; shutao_li@hnu.edu.cn; fangleyuan@gmail.com).

X. Jia is with the School of Engineering and Information Technology, University of New South Wales, Canberra, ACT 2610, Australia (e-mail: x.jia@adfa.edu.au).

J. A. Benediktsson is with the Faculty of Electrical and Computer Engineering, University of Iceland, 101 Reykjavík, Iceland (e-mail: benedikt@hi.is).

Color versions of one or more of the figures in this paper are available online at <http://ieeexplore.ieee.org>.

Digital Object Identifier 10.1109/TGRS.2017.2691906

of wavelengths, for the same area of land cover. This type of imagery offers the detailed ground information in both the spectral and spatial domains. Thus, it has been widely used in remote sensing applications, e.g., urban mapping, environment monitoring, object identification, and military defense [1], [2].

In the last decades, hyperspectral image (HSI) classification has been an active area of research in a remote sensing analysis domain. Discriminative approaches have been widely developed in the literature. For instance, the support vector machine (SVM) [3] and the multinomial logistic regression (MLR) [4] are among the most widely used classifiers for HSI, which categorize pixels in the image scene according to spectral similarity between test and training samples.

However, one important problem in the HSI classification domain, i.e., the presence of mixed pixels, makes accurate classification to be a tough task. That is, if a pixel is highly mixed, it is very difficult to identify spectral signals, since it is not easily separable between different classes. One optional solution to this problem is to develop subpixel-based approaches [5]–[9]. Based on the assumption that each spectral signal reflects the response of multiple underlying materials, different unmixing techniques [10]–[13] have been developed to estimate the abundance fractions (AFs) of pure spectral signals (called as endmembers). With the estimated AFs, the spectral mixture phenomenon of each specific pixel can be described at a subpixel level. Then, the AFs are combined with classical classifiers, e.g., SVM and MLR, to determine the final classification results. Despite the important advances reported in the spectral unmixing literature, it is indicated in [6] and [9] that only a moderate improvement in classification accuracies is presented if only the unmixing-based spectral composition information is considered. This should own to the difficulties in determining the exact number of spectral endmembers and properly identifying the pure spectral components, especially when the scene is dominated by both noisy and mixed pixels. Therefore, it is essential to integrate other complementary information or fusing multiple classifiers for more robust and accurate classification results, instead of only relying on the spectral unmixing technique.

In addition, the increase in spectral intraclass variability and the decrease in interclass separation also make it difficult to distinguish between different land covers. To improve the discrimination, it is of great interest to develop effective spatial–spectral feature extraction techniques and spectral–spatial classifiers [14]–[18]. Among them, a trend has been

oriented toward to the investigation of morphological profile (MP)-based features, which are built via the dimension reduction and morphological transformation. The introduction of the MP to deal with the HSI classification is initially proposed in [15] and [17]. Inspired by the works in [15] and [17], more variance of the MP has been widely investigated in the literature [19]–[21]. For instance, a compact representation of the MP was obtained in [19] by calculating the differential MP (DMP), which can reflect the variance between pixel and its surroundings. The use of the MP-based features can exploit the spatial structure and geometry information for better classification results, which have also been included in some multifeature fusion works [22], [23]. However, a main limitation of the MP-based features is that they rely only on a few extracted components, e.g., the first few components via the principal component analysis (PCA) [24], which do not fully utilize the spectral information in the HSI.

Recently, the superpixel-based HSI classification methods attract much attention [25]–[30], which have demonstrated effective in providing significant advantages to improve the classification performance. Generally, each superpixel in HSI corresponds to a set of spatially connected and spectrally similar pixels within a shape-adaptive homogeneous region, which can be accomplished via the oversegmentation methods [31]–[33]. After generating all the superpixels, one option to assign the label for each superpixel is to combine the pixelwise classification results and fusion rules. For instance, with the majority voting (MV) rule, all pixels within one superpixel are assigned to the most frequent class within this region. More advanced works accomplish this process of a label assignment, according to a distance metric measured between pixels within each superpixel and each class of training samples. For example, the works in [26] and [27] construct the distance metric based on extended sparse representation models, i.e., discriminative sparse model [26] and multitask joint sparse model [27]. In [29], a set-to-set distance is introduced based on the affine hull representation. These approaches always present superiority in the classification performance over the MV-based fusion strategy, due to the joint use of both the spectral and the spatial information in the process of classification. However, wrong label estimation cannot be avoided if one superpixel contains more than one category of spectral signals, due to the one label for one-superpixel manner.

Based on the aforementioned analysis, it can be concluded that the three types of features, i.e., subpixel-level spectral mixture feature, pixel-level structure feature, and superpixel-level spatial–spectral similarity feature, can characterize the hyperspectral data from different aspects, as shown in Fig. 1. Thus, a novel framework is proposed to integrate the complementary information that is offered by each of the three features, in this paper. By this way, it is able to take advantage of multiple features and eliminate the drawbacks of the conventional techniques that evolve each feature independently. Despite the developed multifeature fusion works [34]–[36] and multiclassifier fusion systems [37]–[39] for the HSI classification in the literature, this is the first time to combine the subpixel-level, pixel-level, and superpixel-level features in one

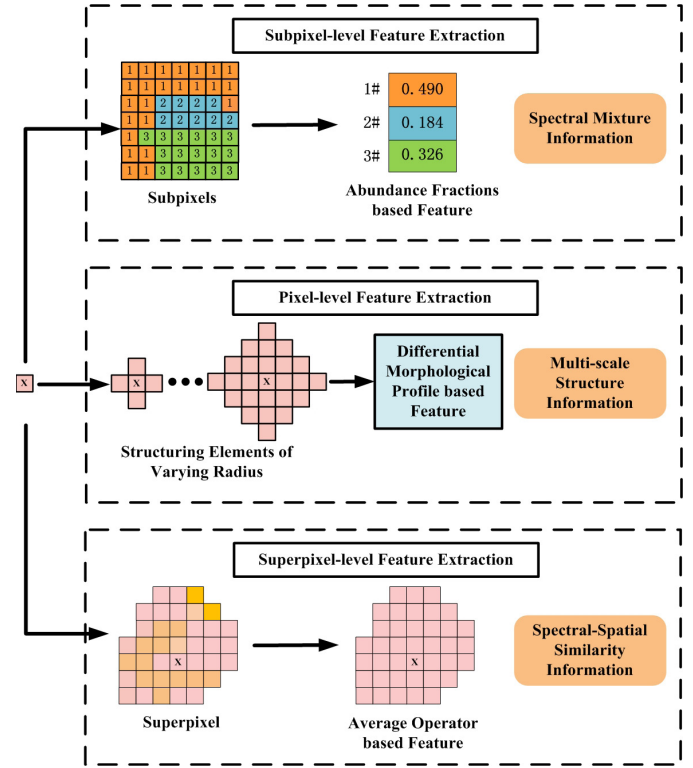


Fig. 1. Illustration of subpixel-, pixel-, and superpixel-based complementary information.

framework. Specifically, an unsupervised spectral unmixing technique is used to estimate the AFs of endmembers (pure spectral), which can model the spectral mixture information at a subpixel level. Besides, the DMP-based operator is applied to extract the structure and geometry information, which can reflect the pixel variance in neighborhood. In addition, shape-adaptive homogeneous regions are generated to extract the similar spectral–spatial information from a superpixel perspective. Then, both composite-kernel-based feature fusion and probabilistic decision fusion schemes are presented for a final label assignment, aiming at jointly using the three different features to further increase classification accuracy.

The remainder of this paper is organized as follows. Section II presents the proposed classification approach, including the processes of subpixel-level, pixel-level, and superpixel-level feature extraction, and the introduced schemes of feature fusion and decision fusion. Section III reports the classification results obtained by the proposed fusion schemes using different real hyperspectral data sets. Section IV concludes this paper with some remarks and hints at future research focus.

II. PROPOSED METHOD

The proposed fusion framework for the HSI classification is summarized by the flowchart in Fig. 2. First, three types of features, including the subpixel-level, pixel-level, and superpixel-level features, are extracted from HSI, respectively. Then, both feature fusion and decision fusion schemes are introduced to combine the offered complementary information by different features, resulting in the final classification map. For simplicity, the proposed classification methods that use

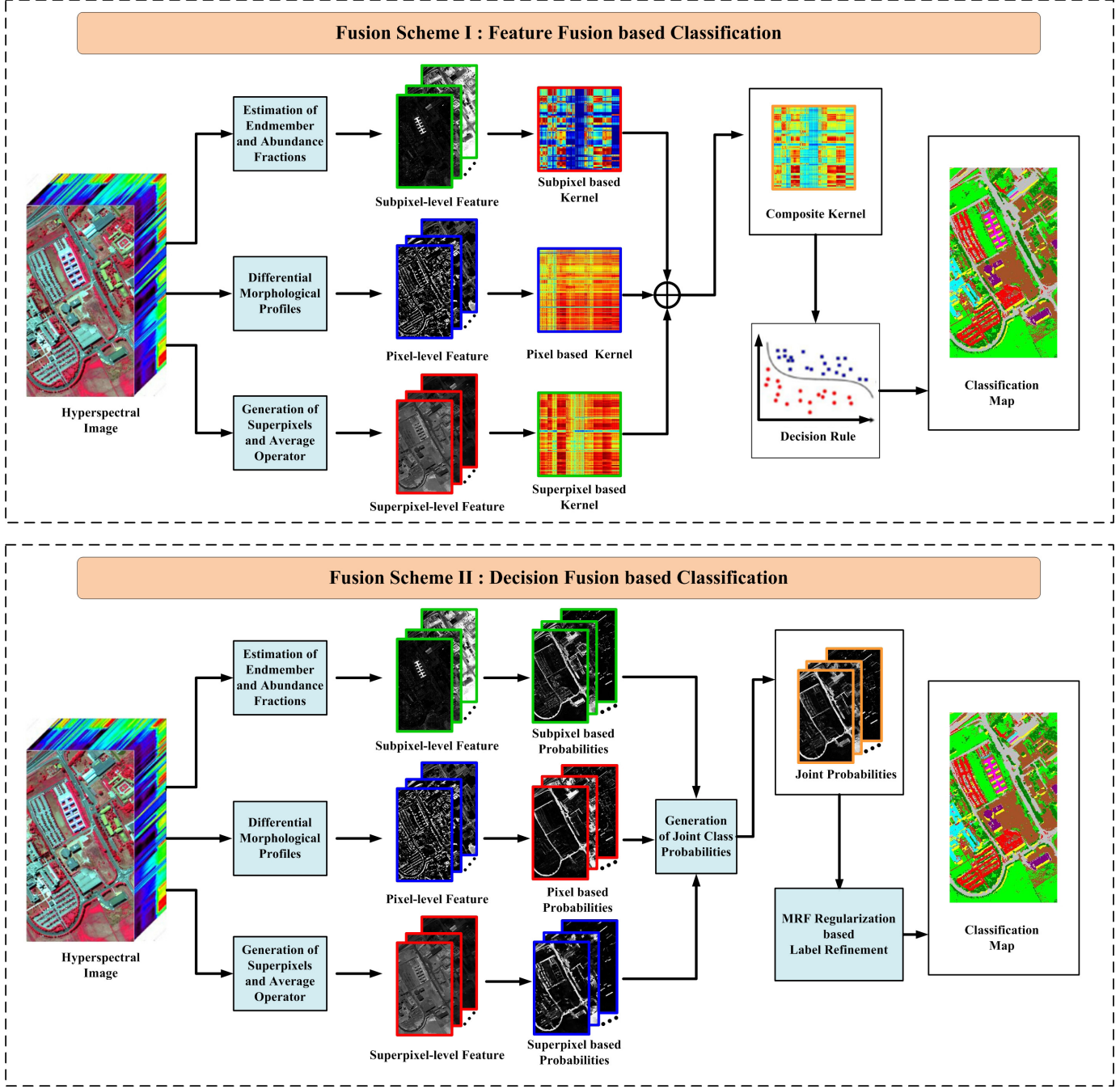


Fig. 2. Proposed fusion schemes to integrate subpixel-, pixel-, and superpixel-based complementary information for HSI classification.

feature fusion and decision fusion to combine the three types of features is shorted by the SPS-FC and SPS-DC, respectively. The detailed descriptions of generating different features and the fusion rules are given in detail as follows.

A. Subpixel-Level Feature Extraction

In the proposed fusion schemes, the subpixel-level feature is represented by fractional abundances, which are estimated via performing the spectral unmixing technique. Here, a well-known linear unmixing model [10] is adopted to characterize spectral mixture in HSI, which is denoted as

$$\mathbf{x}_i = \sum_{e=1}^p \Phi_i^e E_e + n_i \quad (1)$$

where \mathbf{x}_i is a pixel at location i in HSI, p is the number of endmembers, E_e denotes the spectral response of endmember e , Φ_i^e is a scalar value corresponding to the fractional abundance of the endmember e at the pixel \mathbf{x}_i , and n_i is a noise item. It is a very challenging issue to accurately estimate the number of endmembers, p in the HSI. If the estimated $\hat{p} \neq p$, there will be possibilities that not all endmembers are available, leading to the failure of fully constrained linear spectral unmixing methods. Therefore, it is decided to resort to partial unmixing techniques [44]–[46], e.g., mixture-tuned matched filtering (MTMF) [46], which have shown a promising performance in the abundance estimation in this partial unmixing situation. Following the work in [6], we first perform

a minimum noise fraction-based dimensionality reduction and then apply the unsupervised MTMF method to estimate the fractional abundances of spectral endmembers via the orthogonal subspace projection algorithm. Specifically, given a number of endmembers, p , an unsupervised clustering algorithm (i.e., k-means [47]) is used to divide all the pixels into p clusters. By this unsupervised manner, all the spectral information in HSI can be better exploited than individually using the training samples. Then, the centroid of each associated cluster, denoted as E_e ($e = 1, 2, \dots, p$), is regarded as each “endmember.” Finally, the MTMF estimates the AF Φ_i of E_e for each specific \mathbf{x}_i by

$$\begin{aligned} \Phi_i^e &= ((E_e^T \mathbf{R}^{-1} E_e)^{-1} \mathbf{R}^{-1} E_e)^T \mathbf{x}_i \\ \text{s.t., } \mathbf{R} &= \frac{1}{N} \sum_{i=1}^N \mathbf{x}_i \mathbf{x}_i^T \end{aligned} \quad (2)$$

where \mathbf{R} is the correlation matrix, and N is the number of all pixels in HSI. By (2), the fractional abundances, $\Phi_i = [\Phi_i^1, \dots, \Phi_i^p]$, for each pixel \mathbf{x}_i can be estimated. As a result, the subpixel-level spectral mixture feature, $\mathbf{z}_i^{\text{sub}}$, can be generated, $\mathbf{z}_i^{\text{sub}} = \Phi_i$.

B. Pixel-Level Feature Extraction

The pixel-level feature is extracted via the DMPs [19], which is derived from the construction of MPs. First of all, the operation of MP is briefly reviewed here. Specifically, an MP is composed of an opening profile (OP) and a closing profile (CP). The OP with L scales at pixel \mathbf{x}_i forms an L -dimensional image, and so does the CP operator. When conducting the operation of MP to hyperspectral data, the PCA is widely used as a preprocessing step to generate the base images. Since the first three PCs contain the most significant information, they are used to form the base images, denoted as $I = \{I_1, I_2, I_3\}$. Let I_1 represent the first PC, the morphological opening and closing operated on I_1 is denoted as $\gamma(I_1)$ and $\phi(I_1)$, respectively. Considering a family of increasing structural elements (SEs), $Q = \{Q_\lambda : \lambda = 0, \dots, L\}$, where Q_λ represents the varying radius of the disk-shaped scalar values used in the filtering

$$\begin{aligned} MP_\gamma &= \{MP_\gamma^\lambda = \gamma^\lambda(I_1)\} \\ MP_\phi &= \{MP_\phi^\lambda = \phi^\lambda(I_1)\}. \end{aligned} \quad (3)$$

As the derivative of MPs, the DMPs can be regarded as a measurement of the gray value variation of the MPs for every step of an increasing SE series, which can better extract the multiscale structure characteristics. Based on (3), the DMPs can be represented as

$$\begin{aligned} DMP_\gamma(I_1) &= \{|MP_\gamma^\lambda(I_1) - MP_\gamma^{\lambda-1}(I_1)|\} \\ DMP_\phi(I_1) &= \{|MP_\phi^\lambda(I_1) - MP_\phi^{\lambda-1}(I_1)|\} \\ \text{s.t., } \lambda &= 1, \dots, L. \end{aligned} \quad (4)$$

Then, DMP_γ and DMP_ϕ generated from the first three PCs are stacked to represent the structural feature. Finally, a $(3 \times 2L)$ -dimensional feature vector is obtained for each

pixel, represented as

$$\begin{aligned} DMP_I &= \{DMP(I_1), DMP(I_2), DMP(I_3)\} \\ \text{s.t., } DMP(I_1) &= \{DMP_\gamma^\lambda(I_1), DMP_\phi^\lambda(I_1)\} \\ DMP(I_2) &= \{DMP_\gamma^\lambda(I_2), DMP_\phi^\lambda(I_2)\} \\ DMP(I_3) &= \{DMP_\gamma^\lambda(I_3), DMP_\phi^\lambda(I_3)\}. \end{aligned} \quad (5)$$

By this way, the pixel-level structure feature can be represented as $\mathbf{z}_i^{\text{pix}} = DMP_I(\mathbf{x}_i)$.

C. Superpixel-Level Feature Extraction

To extract a superpixel-level feature, the first step is to oversegment the whole image into multiple nonoverlapping regions, where each region corresponds to one superpixel. In the literature, there are several popular superpixel segmentation algorithms [31], [40]–[43]. Among them, the watershed [40] and mean-shift [41] methods produce superpixels with irregular sizes and shapes, which tend to straddle multiple objects. The tubopixel algorithm [42] involves boundary curves in the image to generate superpixels of a similar regularity, and the work in [43] achieves the superpixel segmentation through solving a GraphCut problem. Nevertheless, the tubopixel and GraphCut methods tend to sacrifice fine image details for their preference of smooth boundaries in the segmentation maps [31]. Furthermore, by combining the entropy rate of a random walk on a graph and a balancing term into one energy function, the entropy rate superpixel (ERS) [31] can better balance the regularization of superpixel shapes and the homogeneity of each superpixel. Therefore, the ERS is adopted for oversegmentation in this paper. Based on the first three PCs extracted via operating the PCA, the ERS generates a subset of edges $E_s \in E$ by solving a graph optimization problem, denoted as

$$\max_{E_s} \{H(E_s) + \lambda F(E_s)\}, \quad \text{s.t., } E_s \in E \quad (6)$$

where H is the entropy rate of the random walk on graph G , and F is a balancing term that encourages clusters with similar sizes and reduces the number of unbalanced superpixels. Based on the subset of edges E_s , one superpixel map, S , can be generated, which oversegments the spatial area into multiple homogeneous patches. Then, each superpixel can be obtained by grouping the spectral pixels within each homogeneous patch S_i . Since pixels in each superpixel are spatially spectrally similar, it is suggested to calculate the average spectral to characterize the common spectral–spatial information. Let M_i represent the number of pixels within S_i , the mathematical definition for this superpixel-level feature extraction can be represented as

$$\mathbf{z}_i^{\text{sup}} = \frac{1}{M_i} \sum_{i \in S_i} \mathbf{x}_i. \quad (7)$$

D. Feature Fusion of Complementary Information

Here, the composite-kernel-based classifier is introduced to effectively combine different features. As the most widely used kernel, the radial basis function kernel is adopted to construct the different kernels, K^{sub} , K^{pix} , and K^{sup} . Take the

subpixel-level feature, \mathbf{z}_i , as an example, the related kernel is calculated by

$$K^{\text{sub}}(\mathbf{z}_i^{\text{sub}}, \mathbf{z}_j^{\text{sub}}) = \exp \frac{(-\|\mathbf{z}_i^{\text{sub}} - \mathbf{z}_j^{\text{sub}}\|^2)}{2\sigma^2} \quad (8)$$

where $\exp(\cdot)$ is an exponential operator. Similarly, the pixel-level and superpixel-level feature kernels can also be constructed, denoted as $K^{\text{pix}}(\mathbf{z}_i^{\text{pix}}, \mathbf{z}_j^{\text{pix}})$ and $K^{\text{sup}}(\mathbf{z}_i^{\text{sup}}, \mathbf{z}_j^{\text{sup}})$, respectively. Then, a composite kernel by averaging these three kernels can be generated

$$K^{\text{sps}}(\mathbf{z}_i, \mathbf{z}_j) = \mu_1 K^{\text{sub}}(\mathbf{z}_i^{\text{sub}}, \mathbf{z}_j^{\text{sub}}) + \mu_2 K^{\text{pix}}(\mathbf{z}_i^{\text{pix}}, \mathbf{z}_j^{\text{pix}}) + \mu_3 K^{\text{sup}}(\mathbf{z}_i^{\text{sup}}, \mathbf{z}_j^{\text{sup}}) \quad (9)$$

where μ_j ($j \in [1, 2, 3]$) are the weights of different kernels, which are uniformly distributed in this paper, $\mu_1 + \mu_2 + \mu_3 = 1$. By applying the composite kernel in (9), K^{sps} , the SVM-based [48] decision rule for each specific pixel can be determined as follows:

$$f(\mathbf{x}) = \sum_{i=1}^{N_{\text{tr}}} c_i a_i K^{\text{sps}}(\mathbf{x}, \mathbf{z}_i) + b \quad (10)$$

where N_{tr} is the number of training samples, a_i is the Lagrange multiplier, c_i is the label for the i th test sample \mathbf{z}_i , and b is the estimation bias.

E. Decision Fusion of Complementary Information

The pairwise SVM classifier [48] is first used to estimate the initial class probabilities based on different features, denoted as p^{sub} (subpixel-level feature), p^{pix} (pixel-level feature), and p^{sup} (superpixel-level feature), respectively. To adaptively combine these class probabilities, certainty degree of class probabilities (CDCPs) and the confidence score of classifiers (CSCs) are introduced, which are described in detail as follows.

1) Certainty Degree of Class Probabilities: The CDCPs [37], [49] is used to indicate the classification certainties for each specific pixel relied on different features. Based on the probability estimation, it is believed that a lower certainty degree should be assigned to the class estimation if probabilities are uniformly distributed. In turn, larger gaps between estimated probabilities indicate a higher discriminative capability between different classes for the current pixel. Take the class probabilities by the subpixel-based estimation as an example, all the probabilities related to a pixel \mathbf{x}_i are first sorted in a descending order, denoted as $\{p_1^{\text{sub}}, p_2^{\text{sub}}, \dots, p_C^{\text{sub}}\}$. The similar operations are also conducted on the pixel-level and superpixel-level features to generate the sorted probability vectors. Then, the CDCPs for estimating the class of pixel \mathbf{x}_i are defined as

$$\begin{aligned} d_i^{\text{sub}} &= p_1^{\text{sub}} - \frac{1}{C-1} \sum_{c=2}^{c=C} p_c^{\text{sub}} \\ d_i^{\text{pix}} &= p_1^{\text{pix}} - \frac{1}{C-1} \sum_{c=2}^{c=C} p_c^{\text{pix}} \\ d_i^{\text{sup}} &= p_1^{\text{sup}} - \frac{1}{C-1} \sum_{c=2}^{c=C} p_c^{\text{sup}} \end{aligned} \quad (11)$$

where C is the number of classes, and d_i^{sub} , d_i^{pix} , and d_i^{sup} represent the CDCPs related to the subpixel-level, pixel-level, and superpixel-level features, respectively.

2) Confidence Score of Classifiers: The introduction of CSCs aims at adaptively assigning appropriate nonuniform scores to each classifier based on different features, according to the capability in discriminating various materials. Let the CSCs represent as $\alpha = \{\alpha^{\text{sub}}, \alpha^{\text{pix}}, \alpha^{\text{sup}}\}$, where α^{sub} , α^{pix} , and α^{sup} are related to the subpixel-level, pixel-level, and superpixel-level features. This way, the weaker classifier relied on less-discriminative feature will be assigned a lower weight, and vice versa. For the estimation of α , the training samples are uniformly divided into two parts, where one part is used to train the classifier, and the other is used to test the classification performance. Let the overall accuracies by an SVM classifier with the subpixel-level, pixel-level, and superpixel-level features be represented as OA_{sub} , OA_{pix} , and OA_{sup} , respectively. Then, the corresponding classifier weight is calculated by

$$\alpha^{\text{sub}} = OA_{\text{sub}}, \alpha^{\text{pix}} = OA_{\text{pix}}, \alpha^{\text{sup}} = OA_{\text{sup}}. \quad (12)$$

Then, both the estimated CDCPs and CSCs are used to generate joint class probabilities for \mathbf{x}_i , defined as

$$\begin{aligned} p_i^{\text{sps}} &= \frac{d_i^{\text{sub}} \alpha^{\text{sub}}}{z_i} p_i^{\text{sub}} + \frac{d_i^{\text{pix}} \alpha^{\text{pix}}}{z_i} p_i^{\text{pix}} + \frac{d_i^{\text{sup}} \alpha^{\text{sup}}}{z_i} p_i^{\text{sup}} \\ \text{s.t., } z_i &= d_i^{\text{sub}} \alpha^{\text{sub}} + d_i^{\text{pix}} \alpha^{\text{pix}} + d_i^{\text{sup}} \alpha^{\text{sup}}. \end{aligned} \quad (13)$$

Based on the joint probabilities, one easy way to determine the final classification estimation for \mathbf{x}_i is according to the maximum probability. However, wrong label assignment for some isolate pixels will appear when very bad probability estimation results are obtained by some of the three classifiers. Following our previous work [39], it is suggested to refine the final classification results via incorporating the Markov random field (MRF) regularization. In the MRF-based framework, the task of final label refinement can be typically represented as a minimization of an energy function, denoted by

$$\hat{\mathbf{Y}} = \min \left\{ \sum_{\mathbf{x}_i \in \mathbf{X}} D_i(\mathbf{x}_i) + \beta \sum_{i, j \in N_i} V_{ij}(y_i, y_j) \right\}. \quad (14)$$

In (14), the data item can be rewritten as $D_i(\mathbf{x}_i) = -\log \hat{p}_i^{\text{sps}}$. The spatial item $V_{ij}(y_i, y_j)$ is calculated by $V_{ij}(y_i, y_j) = 1 - \delta(y_i, y_j)$, where $\delta(\cdot, \cdot)$ is the Kronecker delta function ($\delta(a, b) = 1$ if $a = b$, and $\delta(a, b) = 0$ otherwise). The parameter β is used to balance both the data item and the spatial item. The class labels can be obtained by minimizing (14) with graph-cut-based optimization algorithm¹ in an iterative manner [50]–[52]. In each iteration, the minimum cut is used to optimally select a set of image pixels to change their labels to a given label. By this way, the value of energy cost function can be reduced gradually. Along with the iterations, the final classification result, $\hat{\mathbf{Y}}$, is obtained, if any change of the labels will no longer lead to further minimization of the energy cost function in (14). More details of the solution to (14) in the context of HSI classification are thoroughly

¹<http://www.wisdom.weizmann.ac.il/~bagon>

described in our previous work [39], as well as in some related works [51]–[53].

III. EXPERIMENTAL RESULTS AND DISCUSSION

A. Hyperspectral Data Sets

Four HSIs, including the “ROSIS-03 University of Pavia,” “AVIRIS Indian Pines,” “Houston University,” and “Pavia Center,” are used to test the performance of the proposed classification method.

1) *University of Pavia*: The “University of Pavia” image was acquired by the ROSIS-03 sensor over the campus at the University of Pavia, Italy. This image contains 103 spectral bands after discarding the seriously noisy bands, and each band is of size 610×340 . The spatial resolution of this image is 1.3 m, and the spectral coverage ranges from 0.43 to 0.86 μm .

2) *AVIRIS Indian Pines*: The “AVIRIS Indian Pines” image, which covers the agricultural Indian Pines test site in Northwestern Indiana, was collected by the airborne visible infrared imaging spectrometer (AVIRIS) sensor. This image is of size $145 \times 145 \times 220$, which has a spatial resolution of 20 m and a spectral range from 0.2 to 2.4 μm . Before the classification, 20 spectral bands (i.e., 104th–108th, 150th–163rd, and 220th) are discarded due to the water absorption.

3) *Houston University*: The “Houston University” image was acquired over the Houston University campus and its neighboring area, which was distributed by the 2013 GRSS Data Fusion Contest. It contains 144 spectral bands in the 380–1050 nm region, and 349×1905 pixels with a spatial resolution of 2.5 m. Heavy shadows contained in the observed data were removed, and a subregion sized 349×1300 was retained for classification. This image is an urban data set, with most of the land covers consisting of man-made objects.

4) *Pavia Center*: The third data set was also collected by the ROSIS optical sensor over a different location in the city center of Pavia, Italy. The flight was also operated by DLR in the HySens framework. The number of data channels in the acquired image is 102 (with a spectral range from 0.43 to 0.86 μm), and the spatial resolution is again 1.3 m per pixel. This image is used in the 2008 IEEE Geoscience and Remote Sensing Data Fusion Technical Committee contest due to rich structures and details are contained in this image.

B. Parameter Discussion

The parameter setting in the proposed fusion schemes for the HSI classification is given as follows. To construct the pixel-level structure feature, the radii of the disk-shaped SEs in (3) are empirically varied starting from 1 with a step size of 2, and the scale number, L , in (4) is set to be 10. To extract the subpixel-level feature, the number of clusters, p , is set to be $2 \times C$, where C is the number of classes in the HSI image. In addition, another two important parameters, N_c (used for determining the number of superpixels) and β (used to balance the data item and spatial item in (14)), should be predefined. Here, the effect of these two parameters on

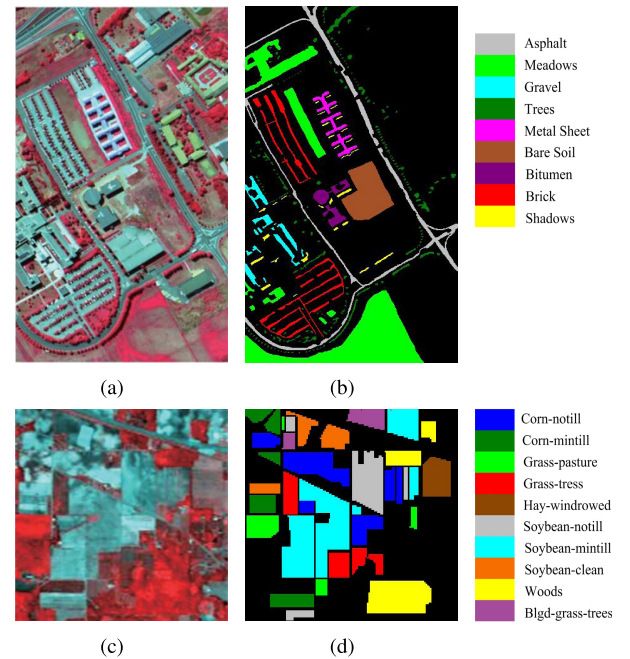


Fig. 3. False-color composite images and reference maps for (a) and (b) University of Pavia image and (c) and (d) Indian Pines image.

TABLE I
NUMBERS OF SAMPLES IN DIFFERENT CLASSES IN THE UNIVERSITY OF PAVIA IMAGE AND INDIAN PINES IMAGE

University of Pavia			Indian Pines		
Class	Name	Number	Class	Name	Number
1	Asphalt	6631	1	Corn-notill	1428
2	Meadows	18649	2	Corn-mintill	830
3	Gravel	2099	3	Grass-pasture	483
4	Trees	3064	4	Grass-tress	730
5	Metal sheet	1345	5	Hay-windrowed	478
6	Bare Soil	5029	6	Sybean-notill	972
7	Bitumen	1330	7	Sybean-mintill	2455
8	Bricks	3682	8	Sybean-clean	593
9	Shadows	947	9	Woods	1265
Total			Total		
42776			9620		

the classification performance is analyzed by evaluating the classification accuracies on two widely used test data sets, “University of Pavia” and “AVIRIS Indian Pines” (as shown in Fig. 3). The reference classes are shown in Table I, and the reference maps are given in Fig. 3. For each test image, a balanced training set was constructed by randomly choosing varying pixels, with the number of training samples for each class (M_{tr}) varying between a range of [10, 30, 50]. The overall classification accuracies, in terms of the overall accuracy (OA), average accuracy (AA), and kappa coefficient (k), are shown in Fig. 4.

In terms of the parameter β , it is easy to notice from Fig. 4 that the classification accuracies can be improved obviously when growing the value of β from 0 to 0.5. This demonstrates that the introduction of the spatial item in (14) can effectively correct some wrong labels, leading to the improvement of the overall classification result. In addition, decrease or unstable

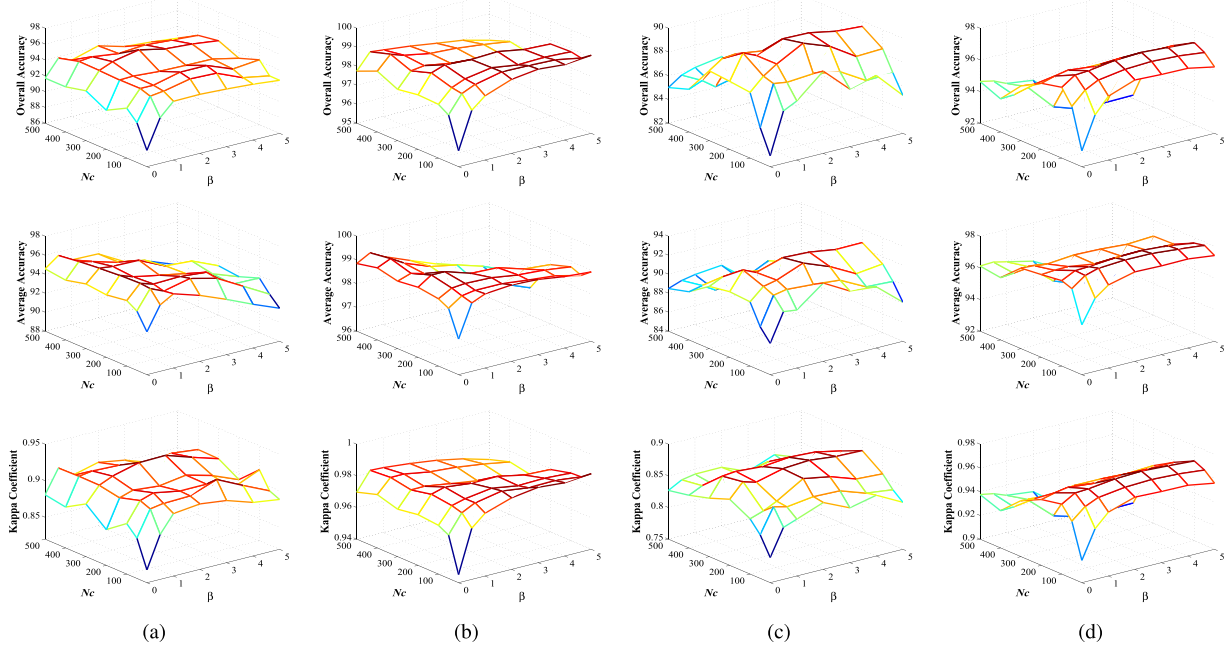


Fig. 4. Effect of the parameters, N_c and β , on the proposed SPS-DC method. Classification accuracies of (a) and (b) University of Pavia image and (c) and (d) Indian Pines image when varying the number of samples for each class ($M_{tr} \in [10, 50]$) are used for training.

trend will appear when continuing to increase β to be values that are larger than 1, especially when training samples are limited, i.e., $M_{tr} = 10$. This is because larger value of β may lead to an oversmoothing classification map. In the following experiments, $\beta = 1$ is set to be the default parameter, since this setting can result in high classification accuracies with varying numbers of training samples for different data sets.

Another parameter, N_c , is used to determine the number of superpixels. Let $M \times N$ represent the spatial size of test HSI image, the predefined number of superpixel is set to be $(M \times N/N_c)$. Generally, a smaller value of N_c determines a larger number of superpixels, leading that each superpixel contains more pixels, and vice versa. However, a much larger N_c value easily leads under segmentation. In addition, too much smaller value of N_c may cause that each superpixel cannot provide enough spatial information for expected classification. Therefore, an appropriate estimation for the number of superpixels is important for an accurate classification. Take a closer look at Fig. 4, it can be seen that the data set of Pavia University prefers a larger value of N_c for a better classification result, but a much larger N_c value will lead to an obvious accuracy reduction for the data set of Indian Pines. This is reasonable since the characters of these two image scenes varied largely, and the Indian Pines image mainly contains homogenous areas, while the University of Pavia consists of more structures and details. In common, relative high classification accuracies can be obtained by setting N_c as the values between a range of [100, 300]. Thus, N_c is set to be 100 for the rest of experiments.

C. Effect of Combining Multiple Features for Classification

In this section, the complementary properties of the aforementioned multiple features and the necessity of combining

multiple features are investigated. According to the related descriptions in Section II, each individual subpixel-level, pixel-level, and superpixel-level feature combined with the SVM classifier is used to estimate the labels for all pixels in the scene. Besides, the three types of features are integrated in both the proposed feature fusion-based classifier and decision fusion-based classifier, i.e., the SPS-FC and SPS-DC. To objectively evaluate the classification results, three metrics of the OA, AA, and k coefficient are used. Besides, the standard deviation (SD) of the classification accuracies over ten runs (shorted by the OA-SD, AA-SD, and κ -SD, respectively) is also reported, to demonstrate the robustness of the proposed method.

From Fig. 5, it can be seen that the classification performance by the subpixel-based classifier (SUB-C), pixel-based classifier (PIX-C), and superpixel-based classifier (SUP-C) varies in different data sets. For the University of Pavia image, the superpixel-level and pixel-level feature outperforms the subpixel-level feature in terms of class discrimination. But with the decrease of training samples, the classification results by the PIX-C, SUB-C, and SUP-C are becoming competitive. When it comes to the Indian Pines image, the superpixel-level feature dominates the advantage, which always presents higher classification accuracies than the result that is dependent on each of the other two features. This should own to that homogeneous regions occupy the majority in the scene of Indian Pines, while more structural details are contained in the University of Pavia. Besides, it can be concluded that the advantages taken by integrating three types of features are more obvious in the case of $M_{tr} = 10$. This exposes one appealing property of the proposed fusion schemes in classifying HSIs, when limited training samples are available. Overall, the proposed fusion frameworks can always

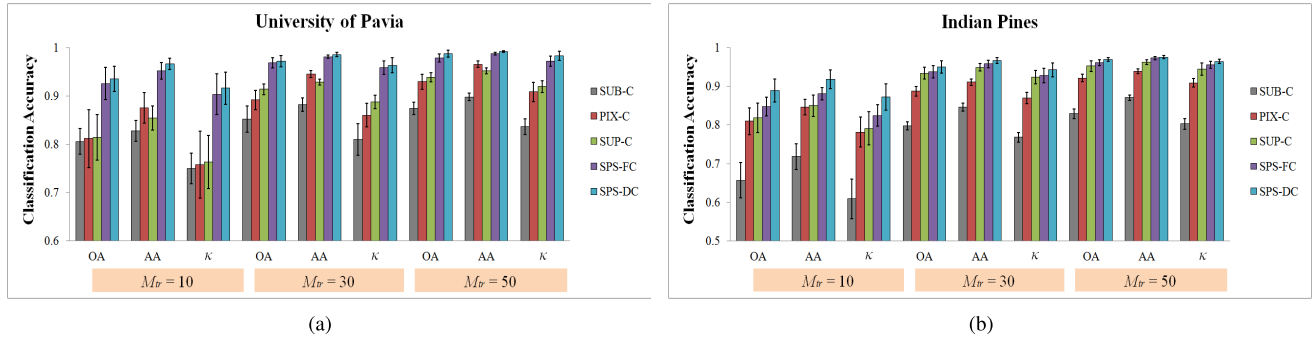


Fig. 5. Classification results of (a) University of Pavia image and (b) Indian Pines image based on different features and fusion schemes. The training samples for each class vary between 10 and 50, $M_{tr} \in [10, 30, 50]$.

TABLE II

CLASSIFICATION ACCURACIES (%) OF THE UNIVERSITY OF PAVIA IMAGE WITH THE SUB-C, PIX-C, SUP-C, SPS-FC, AND SPS-DC METHODS

Class	Train	Test	SUB-C	PIX-C	SUP-C	SPS-FC	SPS-DC
1	10	6621	73.97	83.63	82.77	93.84	96.88
2	10	18639	81.98	76.06	78.54	90.57	89.21
3	10	2089	72.09	87.91	76.51	96.08	98.12
4	10	3054	88.19	89.66	83.03	94.90	94.44
5	10	1335	97.65	99.57	98.50	99.31	99.34
6	10	5019	88.34	71.61	85.43	91.76	96.54
7	10	1320	81.58	99.68	90.63	99.33	99.94
8	10	3672	61.58	88.93	75.78	90.81	95.62
9	10	937	99.51	90.72	97.82	100	99.80
OA		80.55	81.16	81.41	92.57	93.50	
(OA-SD)		(2.67)	(5.99)	(4.75)	(3.36)	(2.65)	
AA		82.76	87.53	85.45	95.18	96.65	
(AA-SD)		(2.14)	(3.18)	(2.52)	(1.73)	(1.24)	
κ		0.750	0.758	0.763	0.904	0.916	
(κ -SD)		(0.032)	(0.069)	(0.055)	(0.042)	(0.033)	

obtain the best results in terms of classification accuracies when all the considered features were combined. This is expected because subpixel-level, pixel-level, and superpixel-level features provide complementary information, which can be jointly exploited with the proposed fusion schemes for better classification results.

In addition, the classification accuracies for each specific class in these two data sets are presented in Tables II and III, to further demonstrate the effectiveness of the proposed fusion schemes in improving class-specific separation. Here, ten samples per class are selected for training and the rest samples are used for testing, i.e., $M_{tr} = 10$. Due to that these three types of features can reflect the discriminative information of HSIs in different aspects, these features have their own advantages and disadvantages in categorizing various classes. Take the University of Pavia image for example. The classification accuracy for the third category with the pixel-level feature is 87.91%, while the results based on each of the other two features are 72.09% and 76.51%, respectively. However, the accuracy generated by PIX-C is only 71.61% when classifying the sixth class, which is less superior to the SUB-C and SUP-C, i.e., 88.34% and 85.43%, respectively. By applying the proposed SPS-FC and SPS-DC schemes, the accuracies for categorizing the third class in the University of Pavia can

TABLE III

CLASSIFICATION ACCURACIES (%) OF THE INDIAN PINES IMAGE WITH THE SUB-C, PIX-C, SUP-C, SPS-FC, AND SPS-DC METHODS

Class	Train	Test	SUB-C	PIX-C	SUP-C	SPS-FC	SPS-DC
1	10	1418	56.83	63.65	80.37	74.26	83.15
2	10	820	57.93	83.82	71.16	80.77	86.57
3	10	473	86.15	89.98	94.76	96.58	96.77
4	10	720	90.50	90.31	95.40	95.67	97.13
5	10	468	98.93	99.72	100	99.98	100
6	10	962	62.49	67.82	69.80	80.30	83.43
7	10	2445	48.60	75.15	75.61	78.08	82.49
8	10	583	69.45	81.61	83.79	87.80	92.33
9	10	1255	79.58	96.72	89.31	95.79	96.88
10	10	376	67.77	92.85	89.73	91.84	99.76
OA		65.66	80.47	81.86	84.77	88.89	
(OA-SD)		(4.59)	(3.47)	(3.83)	(2.40)	(3.23)	
AA		71.82	84.16	84.99	88.11	91.85	
(AA-SD)		(3.31)	(2.05)	(2.81)	(1.56)	(2.47)	
κ		0.609	0.776	0.791	0.825	0.872	
(κ -SD)		(0.051)	(0.039)	(0.043)	(0.028)	(0.036)	

achieve up to 96.08% and 98.12%, and meanwhile 91.76% and 96.54% for the sixth class, respectively. Overall, the proposed fusion schemes can generate higher accuracies for the majority of classes (eight out of nine classes in the University of Pavia image and all classes in the Indian Pines image), when compared with the results relied on each of the three features only. This can demonstrate the effectiveness of the proposed fusion schemes in the improvement of classification results, which should benefit from the integration of subpixel-level, pixel-level, and superpixel-level features.

D. Comparison Results by Different Classification Methods

Here, the classification results by the proposed fusion-based methods are visually and quantitatively compared with both the classical and state-of-the-art classifiers, including the SVM [3], shape-adaptive dictionary learning (SADL) [55], generalized composite kernel-based multivariate logistic regression (GCK-MLR) [34], multiple nonlinear feature learning (MNFL) with multivariate logistic regression [23], superpixel-based classification via multiple kernels (SC-MK) [36], decision fusion classification based on joint collaborative representation and SVM (JCR-SVM) models [56], and the probabilistic fusion classification

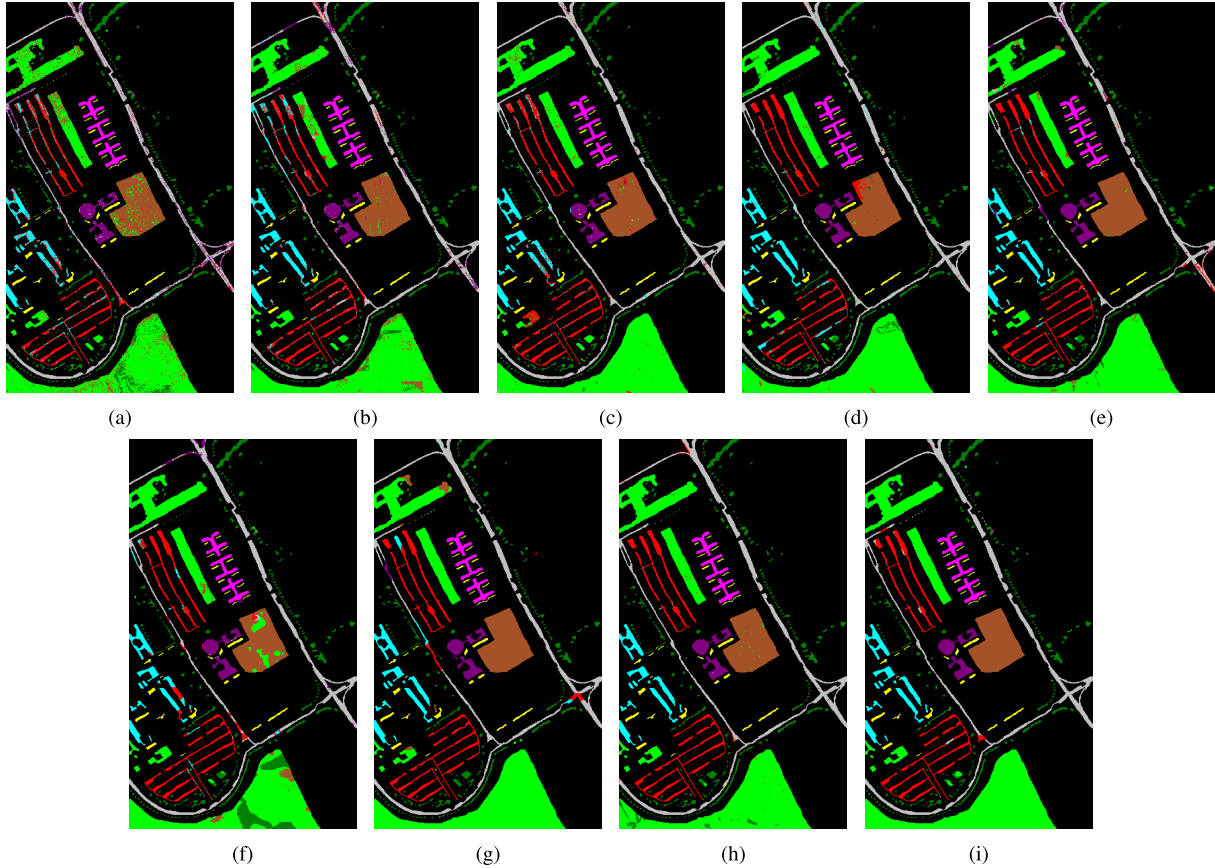


Fig. 6. Classification results for the University of Pavia image with $M_{tr} = 50$. Classification maps generated by different compared methods. (a) SVM [3], OA = 84.17. (b) SADL [55], OA = 91.03. (c) GCK-MLR [34], OA = 96.01. (d) MNFL [23], OA = 95.87. (e) SC-MK [36], OA = 96.20. (f) JCR-SVM [56], OA = 92.13. (g) PSPFC [39], OA = 96.66. (h) SPS-FC, OA = 97.74. (i) SPS-DC, OA = 98.89. The numerical results refer to the overall classification accuracies in percent.

TABLE IV

CLASSIFICATION ACCURACIES (%) OF THE UNIVERSITY OF PAVIA IMAGE WITH THE SVM [3], SADL [55], GCK-MLR [34], MNFL [23], SC-MK [36], JCR-SVM [56], PSPFC [39], SPS-FC, AND SPS-DC METHODS

50 training samples for each class ($M_{tr} = 50$, $N_{tr}/N_{alt} \approx 1.05\%$)									
Class	SVM	SADL	GCK-MLR	MNFL	SC-MK	JCR-SVM	PSPFC	SPS-FC	SPS-DC
1	77.23 (3.66)	94.66 (2.28)	96.40 (1.60)	96.71 (1.27)	93.86 (3.03)	94.08 (1.37)	90.26 (3.00)	97.61 (0.90)	98.66 (1.24)
2	82.73 (4.75)	98.36 (1.09)	96.65 (1.32)	95.32(2.14)	95.38(2.80)	88.97 (2.38)	96.51 (1.61)	96.91 (1.77)	98.23 (1.82)
3	82.54 (2.85)	78.77 (5.29)	89.07 (2.59)	94.30(2.56)	98.26 (1.54)	89.53 (3.20)	98.77 (1.85)	99.38 (0.39)	99.78 (0.18)
4	93.92 (2.14)	88.39 (5.39)	96.22 (1.00)	94.89(1.96)	97.65 (0.96)	96.54 (1.59)	94.97 (2.15)	96.85 (1.63)	97.25 (0.67)
5	99.17 (0.34)	99.98 (0.04)	99.24 (0.59)	99.71 (0.22)	100 (0)	99.89 (0.17)	99.77 (0.12)	99.34 (0.41)	99.86 (0.12)
6	85.09 (4.30)	78.89 (6.56)	97.30 (0.94)	96.85(0.95)	97.07 (3.37)	88.31 (6.14)	99.99 (0.03)	99.49 (0.34)	100 (0)
7	93.44 (2.63)	75.31 (4.47)	97.87 (1.07)	99.52(0.35)	99.75 (0.19)	96.94 (2.07)	99.98 (0.05)	99.71 (0.21)	100 (0)
8	81.67 (4.22)	84.14 (3.39)	92.27 (1.80)	95.05 (1.79)	96.46 (1.75)	91.90 (3.03)	98.43 (1.93)	99.20 (0.61)	99.18 (0.60)
9	99.93 (0.08)	99.72 (0.19)	99.77 (0.20)	99.81 (0.11)	100 (0)	97.09 (1.69)	98.53 (1.32)	99.96 (0.14)	100 (0)
OA (OA-SD)	84.04 (2.20)	90.99 (1.53)	96.09 (0.70)	95.97 (1.00)	96.11 (1.13)	91.25 (1.09)	96.36 (1.02)	97.86 (0.79)	98.73 (0.70)
AA (AA-SD)	88.41 (0.56)	88.69 (1.22)	96.09 (0.39)	96.91 (0.42)	97.60 (0.69)	93.69 (0.51)	97.47 (0.59)	98.72 (0.29)	99.22 (0.18)
$\kappa(\kappa\text{-SD})$	0.794 (0.026)	0.882 (0.019)	0.948 (0.009)	0.947(0.013)	0.949 (0.015)	0.886 (0.014)	0.952 (0.013)	0.972 (0.010)	0.983 (0.009)

method based on pixel-level and superpixel-level classifiers (PSPFC) [39]. Among these compared methods, the SVM is a pixel-level classifier without considering the spatial context, while the rest ones are spectral-spatial classifiers that jointly integrate both the spectral and the spatial information in HSI. Specifically, the SADL [55] method introduces one structural dictionary learning model for the HSI classification, where both spectral information and spatial context are jointly integrated. The GCK-MLR [34], MNFL [23], and SC-MK [36] are based on feature fusion techniques, which combine multiple types of

spectral-spatial features. The JCR-SVM [56] and PSPFC [39] proposed different decision fusion schemes to integrate multiple classification results. The parameters in the GCK-MLR and JCR-SVM are set as the default values. The important parameters for the MNFL, SC-MK, and PSPFC methods are tuned to generate the best classification accuracies for each test image.

Fig. 6 shows the classification maps by different methods for the University of Pavia image, with 50 samples per class being used for training, i.e., $M_{tr} = 50$. From the visual comparison, it can be seen that the proposed decision fusion scheme,

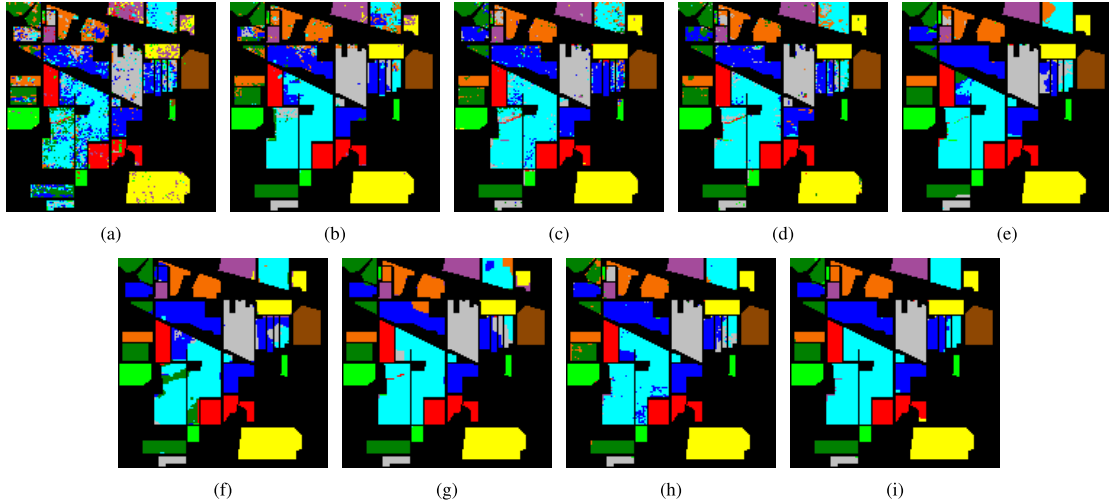


Fig. 7. Classification results for the Indian Pines image with $M_{tr} = 50$. Classification maps generated by different compared methods. (a) SVM [3], OA = 73.36. (b) SADL [55], OA = 88.79. (c) GCK-MLR [34], OA = 91.09. (d) MNFL [23], OA = 91.66. (e) SC-MK [36], OA = 94.95. (f) JCR-SVM [56], OA = 92.41. (g) PSPFC [39], OA = 94.76. (h) SPS-FC, OA = 96.32. (i) SPS-DC, OA = 97.20. The numerical results refer to the overall classification accuracies in percent.

TABLE V

CLASSIFICATION ACCURACIES (%) OF THE INDIAN PINES IMAGE WITH THE SVM [3], SADL [55], GCK-MLR [34], MNFL [23], SC-MK [36], JCR-SVM [56], PSPFC [39], SPS-FC, AND SPS-DC METHODS

Class	50 training samples for each class ($M_{tr} = 50$, $N_{tr}/N_{all} \approx 1.05\%$)								
	SVM	SADL	GCK-MLR	MNFL	SC-MK	JCR-SVM	PSPFC	SPS-FC	SPS-DC
1	62.80 (4.66)	79.48 (3.31)	85.07 (3.24)	85.92 (1.33)	94.46 (3.26)	89.53 (1.96)	89.02 (3.50)	90.15 (4.05)	94.19 (2.41)
2	69.14 (2.83)	81.36 (5.89)	95.38 (1.39)	90.40 (3.32)	96.95 (1.59)	91.44 (4.10)	93.50 (6.25)	98.18 (1.32)	98.22 (1.76)
3	88.43 (3.42)	98.09 (1.93)	94.16 (2.87)	93.09 (2.19)	95.68 (2.22)	96.51 (1.17)	98.23 (2.22)	98.22 (1.79)	98.64 (1.99)
4	92.71 (1.79)	96.00 (1.53)	99.09 (0.47)	99.44 (0.71)	100 (0)	99.85 (0.19)	99.95 (0.09)	99.04 (1.44)	99.47 (0.80)
5	98.79 (1.33)	99.93 (0.16)	100 (0)	99.65 (0.43)	100 (0)	100 (0)	100 (0)	100 (0)	100 (0)
6	73.22 (4.59)	84.53 (3.82)	89.58 (1.82)	87.33 (2.92)	92.38 (2.11)	89.09 (7.37)	95.21 (1.14)	95.54 (1.82)	89.72 (2.77)
7	60.32 (3.64)	95.52 (2.10)	83.64 (3.38)	89.86 (2.26)	91.01 (4.60)	85.78 (4.30)	90.58 (3.77)	94.58 (2.46)	97.19 (2.30)
8	68.97 (5.57)	68.29 (3.08)	94.00 (2.51)	91.73 (3.15)	97.73 (3.64)	98.92 (0.77)	98.62 (1.96)	98.93 (0.51)	98.66 (1.09)
9	87.47 (4.34)	99.38 (0.38)	97.47 (2.19)	97.56 (3.00)	98.53 (2.47)	97.71 (0.75)	97.05 (3.45)	99.70 (0.42)	99.93 (0.03)
10	71.46 (2.98)	84.99 (4.64)	96.31 (1.49)	94.67 (2.36)	97.41 (0.99)	97.51 (1.04)	99.90 (0.66)	99.49 (0.51)	99.73 (0.38)
OA (OA-SD)	72.85 (1.34)	88.62 (1.42)	90.81 (1.21)	91.70 (0.90)	95.13 (1.21)	92.20 (1.41)	94.25 (0.97)	96.20 (0.76)	96.98 (0.54)
AA (AA-SD)	77.33 (1.23)	88.76 (1.21)	93.47 (0.77)	92.97 (0.83)	96.41 (0.57)	94.63 (0.88)	96.21 (0.58)	97.38 (0.42)	97.57 (0.53)
κ (κ -SD)	0.689 (0.015)	0.870 (0.016)	0.890 (0.010)	0.903 (0.010)	0.943 (0.014)	0.909 (0.016)	0.933 (0.011)	0.956 (0.009)	0.965 (0.006)

TABLE VI

NUMBERS OF SAMPLES IN DIFFERENT CLASSES IN THE HOUSTON UNIVERSITY IMAGE AND PAVIA CENTER IMAGE

Houston University					
Class	Name	Number	Class	Name	Number
1	Healthy grass	1073	9	Road	1031
2	Stressed grass	810	10	Highway	382
3	Synthetic grass	697	11	Railway	114
4	Tress	1053	12	Parking Lot1	1233
5	Soil	1242	13	Parking Lot2	449
6	Water	325	14	Tennis court	428
7	Residential	978	15	Running track	660
8	Commercial	624		Total	11099
Pavia Center					
Class	Name	Number	Class	Name	Number
1	Water	65993	6	Asphalt	9248
2	Trees	7598	7	Bitumen	7287
3	Meadows	3104	8	Tiles	42967
4	Bricks	2685	9	Shadow	2863
5	Bare Soil	6584		Total	148329

i.e., SPS-DC, generates a better balance in classifying homogeneous areas and structural edges. Take the meadows and bare soil-related areas (related to the second and sixth classes)

for examples, smoother results in the classification map can be obtained by the SPS-DC than the rest compared methods. In addition, though the GCK-MLR, SC-MK, and PSPFC methods perform better than the proposed SPS-FC in the meadows area (the bottom of the image) from the visual impression, the higher OA (marked in Fig. 6) obtained by the SPS-FC indicates a better classification performance in general. Furthermore, quantitative comparisons in Table IV can confirm the better discriminative capability of the proposed fusion schemes, where N_{tr} is the number of total training samples, and N_{all} is the total number of samples in the reference ground truth. Specifically, the classification accuracies in terms of OA metric by the SPS-FC and SPS-DC methods are 97.86% and 98.73%, respectively, while the rest compared methods have the overall accuracies of less than 97%.

Fig. 7 shows the classification maps of the image of “AVIRIS Indian Pines” by various classification methods. It can be observed that the SVM presents a very noisy estimation in the classification map, exposing the drawbacks of the pixel-level classifiers without incorporating a spatial prior. In contrast, the SADL, GCK-MLR, and MNFL methods can yield a smoother visual effect due to the integration of both the spectral and the spatial information.



Fig. 8. False-color composite images of (a) Houston University and (b) Pavia Center test data sets.

TABLE VII

CLASSIFICATION ACCURACIES (%) OF THE HOUSTON UNIVERSITY IMAGE WITH THE SVM [3], SADL [55], GCK-MLR [34], MNFL [23], SC-MK [36], JCR-SVM [56], PSPFC [39], SPS-FC, AND SPS-DC METHODS

	$M_{tr}=10$ ($N_{tr}/N_{all} \approx 1.35\%$)			$M_{tr}=30$ ($N_{tr}/N_{all} \approx 4.05\%$)			$M_{tr}=50$ ($N_{tr}/N_{all} \approx 6.76\%$)		
	OA (OA-SD)	AA (AA-SD)	κ (κ -SD)	OA (OA-SD)	AA (AA-SD)	κ (κ -SD)	OA (OA-SD)	AA (AA-SD)	κ (κ -SD)
SVM	82.61 (1.37)	83.40 (1.06)	0.811 (0.015)	91.07 (1.27)	91.11 (1.08)	0.903 (0.014)	92.99 (0.41)	93.11 (0.39)	0.924 (0.004)
SADL	87.33 (1.36)	85.93 (1.82)	0.862 (0.015)	93.65 (0.59)	92.36 (0.98)	0.931 (0.006)	96.36 (0.66)	96.15 (0.85)	0.960 (0.007)
GCK-MLR	89.01 (1.42)	89.72 (1.13)	0.880 (0.015)	95.47 (0.56)	95.33 (0.59)	0.951 (0.006)	97.44 (0.34)	97.24 (0.38)	0.972 (0.004)
MNFL	87.28 (2.13)	88.15 (1.80)	0.862 (0.023)	94.93 (1.12)	95.19 (0.96)	0.945 (0.012)	97.16 (0.47)	97.18 (0.33)	0.969 (0.005)
SC-MK	88.70 (1.20)	89.99 (0.72)	0.877 (0.013)	95.55 (0.61)	95.77 (0.46)	0.952 (0.007)	97.28 (0.43)	97.37 (0.41)	0.970 (0.005)
JCR-SVM	91.70 (1.02)	93.36 (0.75)	0.910 (0.011)	94.10 (0.70)	95.54 (0.55)	0.936 (0.008)	94.83 (0.68)	96.06 (0.53)	0.944 (0.007)
PSPFC	87.93 (0.87)	88.98 (1.30)	0.869 (0.009)	95.30 (0.75)	95.54 (0.65)	0.949 (0.008)	97.42 (0.75)	97.49 (0.65)	0.972 (0.008)
SPS-FC	89.67 (1.34)	91.24 (1.17)	0.888 (0.014)	95.35 (0.99)	96.02 (0.69)	0.949 (0.011)	97.34 (0.36)	97.48 (0.34)	0.971 (0.004)
SPS-DC	91.87 (1.42)	92.61 (1.05)	0.912 (0.015)	97.04 (0.81)	97.13 (0.73)	0.968 (0.009)	98.55 (0.42)	98.43 (0.51)	0.984 (0.005)

TABLE VIII

CLASSIFICATION ACCURACIES (%) OF THE PAVIA CENTER IMAGE WITH THE SVM [3], SADL [55], GCK-MLR [34], MNFL [23], SC-MK [36], JCR-SVM [56], PSPFC [39], SPS-FC, AND SPS-DC METHODS

	$M_{tr}=10$ ($N_{tr}/N_{all} \approx 0.06\%$)			$M_{tr}=30$ ($N_{tr}/N_{all} \approx 0.18\%$)			$M_{tr}=50$ ($N_{tr}/N_{all} \approx 0.30\%$)		
	OA (OA-SD)	AA (AA-SD)	κ (κ -SD)	OA (OA-SD)	AA (AA-SD)	κ (κ -SD)	OA (OA-SD)	AA (AA-SD)	κ (κ -SD)
SVM	91.54 (0.54)	86.05 (1.50)	0.882 (0.009)	95.59 (0.33)	91.45 (0.67)	0.938 (0.005)	96.59 (0.38)	92.91 (0.61)	0.950 (0.006)
SADL	96.28 (0.34)	88.59 (1.45)	0.947 (0.005)	97.75 (0.32)	92.77 (0.89)	0.968 (0.005)	98.17 (0.39)	94.18 (1.25)	0.970 (0.006)
GCK-MLR	96.38 (0.53)	92.19 (0.98)	0.949 (0.007)	98.10 (0.33)	96.48 (0.85)	0.973 (0.005)	98.50 (0.38)	97.44 (0.36)	0.979 (0.005)
MNFL	94.58 (1.11)	89.65 (1.50)	0.924 (0.016)	97.25 (0.28)	94.52 (0.83)	0.961 (0.004)	98.10 (0.33)	96.06 (0.56)	0.973 (0.005)
SC-MK	96.03 (0.85)	92.94 (1.22)	0.944 (0.012)	97.51 (0.59)	95.45 (1.06)	0.965 (0.008)	98.15 (0.33)	96.15 (0.45)	0.974 (0.005)
JCR-SVM	97.83 (0.63)	94.63 (1.32)	0.969 (0.009)	98.24 (0.30)	95.37 (0.63)	0.975 (0.004)	98.60 (0.26)	96.27 (0.49)	0.980 (0.010)
PSPFC	96.09 (0.69)	91.36 (1.09)	0.945 (0.010)	97.75 (0.69)	95.45 (1.09)	0.968 (0.010)	98.71 (0.69)	97.38 (1.09)	0.982 (0.010)
SPS-FC	96.95 (0.44)	93.88 (1.05)	0.957 (0.006)	98.44 (0.26)	96.97 (0.45)	0.978 (0.004)	98.72 (0.32)	97.52 (0.41)	0.982 (0.005)
SPS-DC	97.81 (0.44)	95.25 (1.20)	0.970 (0.005)	99.07 (0.24)	97.93 (0.61)	0.987 (0.003)	99.34 (0.25)	98.76 (0.39)	0.991 (0.003)

However, “pepper and noisy” appearance of varied degrees in some homogeneous regions is still noticeable. Since this image mainly consists of large-sized homogeneous regions, the incorporation of superpixel-based information by both the SC-MK and PSPFC, and the introduced fusion schemes present much better classification results than the other compared methods. From the class-by-class accuracies shown in Table V, it can be concluded that the introduced fusion schemes dominate the advantages in classifying the majority of classes (i.e., seven out of ten classes). Furthermore, the better classification results in terms of OA, AA, and κ indexes obtained by the introduced fusion schemes demonstrate the overall superiority.

In addition, another two data sets, “Houston University” and “ROSI Pavia Center,” are used to evaluate the performance of different compared methods. The composite color image of these two data sets is shown in Fig. 8, and the numbers of samples for each class in these two test images are given in Table VI. From the numerical comparison results

in Tables VII and VIII, it can be seen that the JCR-SVM and the SPS-DC present the competitive classification performance when a few training samples are available, i.e., $M_{tr} = 10$. However, the growth of classification accuracies by the JCR-SVM is limited when more training samples are used, especially for the Houston University image. When compared with the rest methods, including the SVM, SADL, GCK-MRL, MNFL, SC-MK, and PSPFC, the proposed SPS-DC always present higher classification accuracies. In addition, another observation is that the SPS-DC always yields a superior performance than SPS-FC in these two data sets. This is because the proposed decision fusion scheme, i.e., SPS-DC, can better take advantage of discriminative properties of three-level features than the proposed SPS-FC.

E. Comparison of Running Time

In this section, the running time for classifying the University of Pavia image and Indian Pines image by different

TABLE IX

RUNNING TIME (SECONDS) OF THE PAVIA UNIVERSITY IMAGE AND INDIAN PINES IMAGE BY THE SVM [3], SADL [55], GCK-MLR [34], MNFL [23], SC-MK [36], JCR-SVM [56], PSPFC [39], SPS-FC, AND SPS-DC METHODS

University of Pavia, $M_{tr} = 50$					
Methods	SVM	SADL	GCK-MLR	MNFL	SC-MK
Time (s)	19.86	261.23	32.05	14.98	57.05
Indian Pines, $M_{tr} = 50$					
Methods	SVM	SADL	GCK-MLR	MNFL	SC-MK
Time (s)	9.37	124.59	17.08	2.29	16.67
Methods	JCR-SVM	PSPFC	SPS-FC	SPS-DC	
Time (s)	89.73	36.69	14.11	48.42	

methods with $M_{tr} = 50$ is reported in Table IX. All the programs are executed on a laptop with an Intel Core i5-4258U and CPU 2.40 GHz on the software platform of MATLAB R2015a.

From Table IX, it can be noticed that the SPS-DC takes more time than the SPS-FC. In the proposed SPS-FC method, one composite kernel is derived from three types of features, which is then used in the SVM classifier for label assignment. However, in the decision fusion scheme, each specific feature is used independently for the estimation of class probabilities, leading to an increase of computational time. In addition, the confidence score of each classifier is estimated based on the classification accuracies of the training samples, again adding more running time. Therefore, the SPS-FC is always more computationally efficient than the SPS-DC. It can also be seen from Table IX that the SADL and JCR-SVM methods always take more running time than the other compared ones. The PSPFC introduces a decision fusion rule to combine classification results by two different classifiers, which is faster than the proposed SPS-DC but slower than the SPS-FC. In addition, since the approaches of the GCK-MLR, MNFL, and SC-MK adopt a similar feature fusion strategy with the SPS-FC, they present competitive performance in terms of running time. Though the proposed fusion-based classification methods are not the most computationally efficient among the compared methods, they can be effectively accelerated via parallel processing. This is reasonable since the steps of extracting different features in the proposed schemes are independent, and meanwhile, the label assignment based on different features in the SPS-DC method is also independent.

IV. CONCLUSION

In this paper, novel frameworks to adaptively integrate the subpixel-, pixel-, and superpixel-based complementary information are proposed for the HSI classification. Here, both the feature fusion and decision fusion schemes are considered. First, the subpixel-level structure feature, pixel-level spectral mixture feature, and superpixel-level spectral-spatial feature are extracted, to characterize varying materials from different aspects. In the feature fusion scheme, three different kernels that are induced from the considered features are added up to generate a composite kernel, which is then incorporated

with an SVM classifier to determine the labels. By this way, each specific feature as well as the cross information between different features can be exploited to improve the discrimination capability. In the decision fusion scheme, each feature is used to estimate the initial class probabilities for each class. Then, the fusion of class probabilities is guided by the CDCPs per each pixel and confidence scores of different classifiers, leading to the final estimation of classification results. With the introduced decision fusion scheme, three types of available features are adaptively integrated for higher classification accuracies. Our experimental results, conducted in four well-known hyperspectral scenes with different spectral and spatial resolutions, indicate that the subpixel-level, pixel-level, and superpixel-level features exhibit great complementarity, which can be used to obtain competitive classification results with regard to other state-of-the-art approaches presented in the literature recently.

Based on the experimental results, one observation is that the introduced decision fusion scheme, i.e., SPS-DC, always outperforms the proposed composite-kernel-based feature fusion way, i.e., SPS-FC. This is due to that the SPS-DC method exhibits more flexibility to combine different types of features than the SPS-FC. For the SPS-DC method, the classification results by using different types of features can be adaptively combined, according to the estimated class probabilities and confidence scores of different classifiers. For the SPS-FC, multiple kernels that are induced from different features share the same weight when constructing the composite kernel for the SPS-FC. Therefore, one focus of the future work will be laid on the development of multikernel learning for more adaptive feature fusion, in order to further improve classification accuracies. In addition, we will improve the computational efficiency of the fusion schemes by using GPU programming and parallel processing.

ACKNOWLEDGMENT

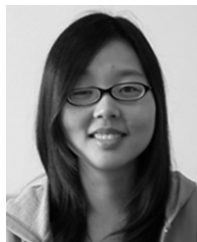
The authors would like to thank Prof. D. Landgrebe from Purdue University and the NASA Jet Propulsion Laboratory for providing the free downloads of hyperspectral data sets. They would also like to thank the Editor-in-Chief, the Associate Editor, and reviewers for their insightful comments and suggestions, which have greatly improved this paper.

REFERENCES

- [1] C.-I. Chang, Ed., *Hyperspectral Data Exploitation: Theory and Applications*. New York, NY, USA: Wiley, 2007.
- [2] J. Pontius, M. Martin, L. Plourde, and R. Hallett, "Ash decline assessment in emerald ash borer-infested regions: A test of tree-level, hyperspectral technologies," *Remote Sens. Environ.*, vol. 112, no. 5, pp. 2665–2676, May 2008.
- [3] F. Melgani and L. Bruzzone, "Classification of hyperspectral remote sensing images with support vector machines," *IEEE Trans. Geosci. Remote Sens.*, vol. 42, no. 8, pp. 1778–1790, Aug. 2004.
- [4] J. Li, J. M. Bioucas-Dias, and A. Plaza, "Semisupervised hyperspectral image segmentation using multinomial logistic regression with active learning," *IEEE Trans. Geosci. Remote Sens.*, vol. 48, no. 11, pp. 4085–4098, Nov. 2010.
- [5] J. W. Boardman and F. A. Kruse, "Analysis of imaging spectrometer data using N -dimensional geometry and a mixture-tuned matched filtering approach," *IEEE Trans. Geosci. Remote Sens.*, vol. 49, no. 11, pp. 4138–4152, Nov. 2011.

- [6] I. Dopido, A. Villa, A. Plaza, and P. Gamba, "A quantitative and comparative assessment of unmixing-based feature extraction techniques for hyperspectral image classification," *IEEE J. Sel. Topics Appl. Earth Observ. Remote Sens.*, vol. 5, no. 2, pp. 421–435, Apr. 2012.
- [7] X. Xu, Y. Zhong, and L. Zhang, "Adaptive subpixel mapping based on a multiagent system for remote-sensing imagery," *IEEE Trans. Geosci. Remote Sens.*, vol. 52, no. 2, pp. 787–804, Feb. 2014.
- [8] A. Villa, J. Chanussot, J. A. Benediktsson, and C. Jutten, "Spectral unmixing for the classification of hyperspectral images at a finer spatial resolution," *IEEE J. Sel. Topics Signal Process.*, vol. 5, no. 3, pp. 521–533, Jun. 2011.
- [9] J. Li, I. Dópido, P. Gamba, and A. Plaza, "Complementarity of discriminative classifiers and spectral unmixing techniques for the interpretation of hyperspectral images," *IEEE Trans. Geosci. Remote Sens.*, vol. 53, no. 5, pp. 2899–2912, May 2015.
- [10] M.-D. Iordache, J. Bioucas-Dias, and A. Plaza, "Sparse unmixing of hyperspectral data," *IEEE Trans. Geosci. Remote Sens.*, vol. 49, no. 6, pp. 2014–2039, Jun. 2011.
- [11] X. Li, X. Jia, L. Wang, and K. Zhao, "On spectral unmixing resolution using extended support vector machines," *IEEE Trans. Geosci. Remote Sens.*, vol. 53, no. 9, pp. 4985–4996, Sep. 2015.
- [12] P. V. Giampouras, K. E. Themelis, A. A. Rontogiannis, and K. D. Kourtoumbas, "Simultaneously sparse and low-rank abundance matrix estimation for hyperspectral image unmixing," *IEEE Trans. Geosci. Remote Sens.*, vol. 54, no. 8, pp. 4775–4789, Aug. 2016.
- [13] N. Keshava and J. F. Mustard, "Spectral unmixing," *IEEE Signal Process. Mag.*, vol. 19, no. 1, pp. 44–57, Jan. 2002.
- [14] X. Kang, S. Li, L. Fang, and J. A. Benediktsson, "Intrinsic image decomposition for feature extraction of hyperspectral images," *IEEE Trans. Geosci. Remote Sens.*, vol. 53, no. 4, pp. 2241–2253, Apr. 2015.
- [15] M. Pesaresi and J. A. Benediktsson, "A new approach for the morphological segmentation of high-resolution satellite imagery," *IEEE Trans. Geosci. Remote Sens.*, vol. 39, no. 2, pp. 309–320, Feb. 2001.
- [16] W. Fu, S. Li, L. Fang, X. Kang, and J. A. Benediktsson, "Hyperspectral image classification via shape-adaptive joint sparse representation," *IEEE J. Sel. Topics Appl. Earth Observ. Remote Sens.*, vol. 9, no. 2, pp. 556–567, Feb. 2016.
- [17] J. A. Benediktsson, J. A. Palmason, and J. R. Sveinsson, "Classification of hyperspectral data from urban areas based on extended morphological profiles," *IEEE Trans. Geosci. Remote Sens.*, vol. 43, no. 3, pp. 480–491, Mar. 2005.
- [18] B. Sun, X. Kang, S. Li, and J. A. Benediktsson, "Random-walker-based collaborative learning for hyperspectral image classification," *IEEE Trans. Geosci. Remote Sens.*, vol. 55, no. 1, pp. 212–222, Jan. 2017.
- [19] P. Ghamisi, M. Dalla Mura, and J. A. Benediktsson, "A survey on spectral-spatial classification techniques based on attribute profiles," *IEEE Trans. Geosci. Remote Sens.*, vol. 53, no. 5, pp. 2335–2353, May 2015.
- [20] R. Bao, J. Xia, M. Dalla Mura, P. Du, J. Chanussot, and J. Ren, "Combining morphological attribute profiles via an ensemble method for hyperspectral image classification," *IEEE Geosci. Remote Sens. Lett.*, vol. 13, no. 3, pp. 359–363, Mar. 2016.
- [21] N. Falco, J. A. Benediktsson, and L. Bruzzone, "Spectral and spatial classification of hyperspectral images based on ICA and reduced morphological attribute profiles," *IEEE Trans. Geosci. Remote Sens.*, vol. 53, no. 11, pp. 6223–6240, Nov. 2015.
- [22] W. Liao, M. Dalla Mura, J. Chanussot, and A. Pižurica, "Fusion of spectral and spatial information for classification of hyperspectral remote-sensed imagery by local graph," *IEEE J. Sel. Topics Appl. Earth Observ. Remote Sens.*, vol. 9, no. 2, pp. 583–594, Feb. 2016.
- [23] J. Li *et al.*, "Multiple feature learning for hyperspectral image classification," *IEEE Trans. Geosci. Remote Sens.*, vol. 53, no. 3, pp. 1592–1606, Mar. 2015.
- [24] G. Hughes, "On the mean accuracy of statistical pattern recognizers," *IEEE Trans. Inf. Theory*, vol. IT-14, no. 1, pp. 55–63, Jan. 1968.
- [25] T. Priya, S. Prasad, and H. Wu, "Superpixels for spatially reinforced Bayesian classification of hyperspectral images," *IEEE Geosci. Remote Sens. Lett.*, vol. 12, no. 5, pp. 1071–1075, May 2015.
- [26] L. Fang, S. Li, X. Kang, and J. A. Benediktsson, "Spectral-spatial classification of hyperspectral images with a superpixel-based discriminative sparse model," *IEEE Trans. Geosci. Remote Sens.*, vol. 53, no. 8, pp. 4186–4201, Aug. 2015.
- [27] J. Li, H. Zhang, and L. Zhang, "Efficient superpixel-level multitask joint sparse representation for hyperspectral image classification," *IEEE Trans. Geosci. Remote Sens.*, vol. 53, no. 10, pp. 5338–5351, Oct. 2015.
- [28] J. Guo, X. Zhou, J. Li, A. Plaza, and S. Prasad, "Superpixel-based active learning and online feature importance learning for hyperspectral image analysis," *IEEE J. Sel. Topics Appl. Earth Observ. Remote Sens.*, vol. 10, no. 1, pp. 347–359, Jan. 2017, doi: 10.1109/JSTARS.2016.2609404.
- [29] T. Lu, S. Li, L. Fang, L. Bruzzone, and J. A. Benediktsson, "Set-to-set distance-based spectral-spatial classification of hyperspectral images," *IEEE Trans. Geosci. Remote Sens.*, vol. 54, no. 12, pp. 7122–7134, Dec. 2016.
- [30] G. Zhang, X. Jia, and J. Hu, "Superpixel-based graphical model for remote sensing image mapping," *IEEE Trans. Geosci. Remote Sens.*, vol. 53, no. 11, pp. 5861–5871, Nov. 2015.
- [31] M.-Y. Liu, O. Tuzel, S. Ramalingam, and R. Chellappa, "Entropy rate superpixel segmentation," in *Proc. IEEE Conf. Comput. Vis. Pattern Recognit.*, Jun. 2011, pp. 2097–2104.
- [32] R. Achanta, A. Shaji, K. Smith, A. Lucchi, P. Fua, and S. Süstrunk, "SLIC superpixels compared to state-of-the-art superpixel methods," *IEEE Trans. Pattern Anal. Mach. Intell.*, vol. 34, no. 11, pp. 2274–2282, Nov. 2012.
- [33] J. Shen, Y. Du, W. Wang, and X. Li, "Lazy random walks for superpixel segmentation," *IEEE Trans. Image Process.*, vol. 23, no. 4, pp. 1451–1462, Apr. 2014.
- [34] J. Li, P. R. Marpu, A. Plaza, J. M. Bioucas-Dias, and J. A. Benediktsson, "Generalized composite kernel framework for hyperspectral image classification," *IEEE Trans. Geosci. Remote Sens.*, vol. 51, no. 9, pp. 4816–4829, Sep. 2013.
- [35] Y. Gu, T. Liu, X. Jia, J. A. Benediktsson, and J. Chanussot, "Nonlinear multiple kernel learning with multiple-structure-element extended morphological profiles for hyperspectral image classification," *IEEE Trans. Geosci. Remote Sens.*, vol. 54, no. 6, pp. 3235–3247, Jun. 2016.
- [36] L. Fang, S. Li, W. Duan, J. Ren, and J. A. Benediktsson, "Classification of hyperspectral images by exploiting spectral-spatial information of superpixel via multiple kernels," *IEEE Trans. Geosci. Remote Sens.*, vol. 53, no. 12, pp. 6663–6674, Dec. 2015.
- [37] X. Huang and L. Zhang, "An SVM ensemble approach combining spectral, structural, and semantic features for the classification of high-resolution remotely sensed imagery," *IEEE Trans. Geosci. Remote Sens.*, vol. 51, no. 1, pp. 257–272, Jan. 2013.
- [38] W. Li, S. Prasad, and J. E. Fowler, "Decision fusion in kernel-induced spaces for hyperspectral image classification," *IEEE Trans. Geosci. Remote Sens.*, vol. 52, no. 6, pp. 3399–3411, Jun. 2014.
- [39] S. Li, T. Lu, L. Fang, X. Jia, and J. A. Benediktsson, "Probabilistic fusion of pixel-level and superpixel-level hyperspectral image classification," *IEEE Trans. Geosci. Remote Sens.*, vol. 54, no. 12, pp. 7416–7430, Dec. 2016.
- [40] D. Comaniciu and P. Meer, "Mean shift: A robust approach toward feature space analysis," *IEEE Trans. Pattern Anal. Mach. Intell.*, vol. 24, no. 5, pp. 603–619, May 2002.
- [41] L. Vincent and P. Soille, "Watersheds in digital spaces: An efficient algorithm based on immersion simulations," *IEEE Trans. Pattern Anal. Mach. Intell.*, vol. 13, no. 6, pp. 583–598, Jun. 1991.
- [42] A. Levinshtein, A. Stere, K. N. Kutulakos, D. J. Fleet, S. J. Dickinson, and K. Siddiqi, "TurboPixels: Fast superpixels using geometric flows," *IEEE Trans. Pattern Anal. Mach. Intell.*, vol. 31, no. 12, pp. 2290–2297, Dec. 2009.
- [43] O. Veksler, Y. Boykov, and P. Mehrani, "Superpixels and supervoxels in an energy optimization framework," in *Proc. Eur. Conf. Comput. Vis.*, 2010, pp. 211–244.
- [44] C.-I. Chang *et al.*, "Generalized constrained energy minimization approach to subpixel target detection for multispectral imagery," *Opt. Eng.*, vol. 39, no. 5, pp. 1275–1281, May 2000.
- [45] J. J. Mitchell and N. F. Glenn, "Subpixel abundance estimates in mixture-tuned matched filtering classifications of leafy spurge (*Euphorbia esula* L.)," *Int. J. Remote Sens.*, vol. 30, no. 23, pp. 6099–6119, Dec. 2009.
- [46] J. Boardman, "Leveraging the high dimensionality of AVIRIS data for improved sub-pixel target unmixing and rejection of false positives: Mixure tuned matched filtering," in *Proc. 5th JPL Geosci. Workshop*, 1998, pp. 55–56.
- [47] D. Arthur and S. Vassilvitskii, "k-means++: The advantages of careful seeding," in *Proc. 18th ACM-SIAM Symp. Discrete Algorithms*, 2015, pp. 1027–1035.
- [48] C.-W. Hsu and C.-J. Lin, "A comparison of methods for multiclass support vector machines," *IEEE Trans. Neural Netw.*, vol. 13, no. 2, pp. 415–425, Mar. 2002.
- [49] Z. Chunsen, Z. Yiwei, and F. Chenyi, "Spectral-spatial classification of hyperspectral images using probabilistic weighted strategy for multifeature fusion," *IEEE Geosci. Remote Sens. Lett.*, vol. 13, no. 10, pp. 1562–1566, Oct. 2016.

- [50] Y. Boykov, O. Veksler, and R. Zabih, "Fast approximate energy minimization via graph cuts," *IEEE Trans. Pattern Anal. Mach. Intell.*, vol. 23, no. 11, pp. 1222–1239, Nov. 2001.
- [51] J. Li, J. M. Bioucas-Dias, and A. Plaza, "Spectral-spatial hyperspectral image segmentation using subspace multinomial logistic regression and Markov random fields," *IEEE Trans. Geosci. Remote Sens.*, vol. 50, no. 3, pp. 809–823, Mar. 2012.
- [52] M. Golipour, H. Ghassemian, and F. Mirzapour, "Integrating hierarchical segmentation maps with MRF prior for classification of hyperspectral images in a Bayesian framework," *IEEE Trans. Pattern Anal. Mach. Intell.*, vol. 54, no. 2, pp. 805–816, Feb. 2016.
- [53] M. Khodadadzadeh, J. Li, A. Plaza, H. Ghassemian, J. M. Bioucas-Dias, and X. Li, "Spectral-spatial classification of hyperspectral data using local and global probabilities for mixed pixel characterization," *IEEE Trans. Geosci. Remote Sens.*, vol. 52, no. 10, pp. 6298–6314, Oct. 2014.
- [54] X. Kang, S. Li, and J. A. Benediktsson, "Spectral-spatial hyperspectral image classification with edge-preserving filtering," *IEEE Trans. Geosci. Remote Sens.*, vol. 52, no. 5, pp. 2666–2677, May 2014.
- [55] A. Soltani-Farani, H. R. Rabiee, and S. A. Hosseini, "Spatial-aware dictionary learning for hyperspectral image classification," *IEEE Trans. Geosci. Remote Sens.*, vol. 53, no. 1, pp. 527–541, Jan. 2015.
- [56] C. Bo, H. Lu, and D. Wang, "Hyperspectral image classification via JCR and SVM models with decision fusion," *IEEE Geosci. Remote Sens. Lett.*, vol. 13, no. 2, pp. 177–181, Feb. 2016.



Ting Lu (S'16) received the B.Sc. degree from Hunan University, Changsha, China, in 2011, where she is currently pursuing the Ph.D. degree.

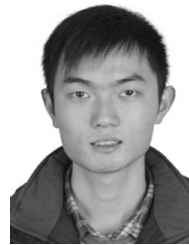
From 2014 to 2015, she was a Visiting Ph.D. Student with the Department of Information Engineering and Computer Science, University of Trento, Trento, Italy, supported by the China Scholarship Council. Her research interests include sparse representation and remote sensing image processing.



Shutao Li (M'07–SM'15) received the B.S., M.S., and Ph.D. degrees from Hunan University, Changsha, China, in 1995, 1997, and 2001, respectively, all in electrical engineering.

In 2001, he joined the College of Electrical and Information Engineering, Hunan University. In 2001, he was a Research Associate with the Department of Computer Science, The Hong Kong University of Science and Technology, Hong Kong. From 2002 to 2003, he was a Post-Doctoral Fellow with the Royal Holloway College, University of London, Surrey, U.K. In 2005, he was a Visiting Professor with the Department of Computer Science, The Hong Kong University of Science and Technology. He is currently a Full Professor with the College of Electrical and Information Engineering, Hunan University. He is also a Chang-Jiang Scholar Professor appointed by the Ministry of Education of China. He has authored or co-authored over 180 refereed papers. In 2013, he was granted the National Science Fund for Distinguished Young Scholars in China. His research interests include compressive sensing, sparse representation, image processing, and pattern recognition.

Dr. Li is a member of the Editorial Board of the *Information Fusion* and the *Sensing and Imaging* journals. He was a recipient of the 2nd-Grade National Award at the Science and Technology Progress of China in 2004 and 2006, respectively. He is an Associate Editor of the IEEE TRANSACTIONS ON GEOSCIENCE AND REMOTE SENSING



Leyuan Fang (S'10–M'14) received the Ph.D. degree in electrical engineering from Hunan University, Changsha, China, in 2015.

From 2011 to 2012, he was a Visiting Ph.D. Student with the Department of Ophthalmology, Duke University, Durham, NC, USA, supported by the China Scholarship Council. Since 2013, he has been an Assistant Professor with the College of Electrical and Information Engineering, Hunan University. His research interests include sparse representation and multiresolution analysis in remote sensing and medical image processing.

Dr. Fang received the Scholarship Award for the Excellent Doctoral Student from the Chinese Ministry of Education in 2011.



Xiuping Jia (M'93–SM'03) received the B.Eng. degree from the Beijing University of Posts and Telecommunications, Beijing, China, in 1982, and the Ph.D. degree in electrical engineering from the University of New South Wales, Sydney, New South Wales, Australia, in 1996.

Since 1988, she has been with the School of Information Technology and Electrical Engineering, University of New South Wales, Canberra Campus, Canberra, ACT, Australia, where she is currently a Senior Lecturer. She is also a Guest Professor with the China University of Petroleum, Beijing, and Harbin Engineering University, Harbin, China, and an Adjunct Researcher with the National Engineering Research Center for Information Technology in Agriculture, Beijing, China. She has authored or co-authored over 160 referred papers, including 65 journal papers. She is the Co-Author of the remote sensing textbook *Remote Sensing Digital Image Analysis* (Springer-Verlag, Third Edition, 1999 and Fourth Edition, 2006). Her research interests include remote sensing, image processing, and spatial data analysis.

Dr. Jia is a Subject Editor of the *Journal of Soils and Sediments* and an Associate Editor of the IEEE TRANSACTIONS ON GEOSCIENCE AND REMOTE SENSING.



Jón Atli Benediktsson (S'84–M'90–SM'99–F'04) received the Cand.Sci. degree from the University of Iceland, Reykjavik, Iceland, in 1984, and the M.S.E.E. and Ph.D. degrees from Purdue University, West Lafayette, IN, USA, in 1987 and 1990, respectively, all in electrical engineering.

He is currently the Rector and a Professor of Electrical and Computer Engineering with the University of Iceland. He is also a Co-Founder of the biomedical start-up company Oxymap, Reykjavik, Iceland. His research interests include remote sensing, biomedical analysis of signals, pattern recognition, image processing, and signal processing. He has authored extensively in those fields.

Dr. Benediktsson is a Fellow of Society of Photo-Optical Instrumentation Engineers. He is a member of the Association of Chartered Engineers, VFI, Iceland, the Societas Scinetiarum Islandica, and the Tau Beta Pi. He was the President of the IEEE Geoscience and Remote Sensing Society (GRSS) from 2011 to 2012. He has been with the GRSS AdCom since 2000. He received the Stevan J. Kristof Award from Purdue University in 1991 as an Outstanding Graduate Student in remote sensing, the Yearly Research Award from the Engineering Research Institute, University of Iceland, in 2006, the Outstanding Service Award from the IEEE GRSS in 2007, and the 2013 IEEE/VFI Electrical Engineer of the Year Award. He was a recipient of the Icelandic Research Councils Outstanding Young Researcher Award in 1997. He was a co-recipient of the University of Iceland's Technology Innovation Award in 2004, the 2012 IEEE TRANSACTIONS ON GEOSCIENCE AND REMOTE SENSING (TGRS) Paper Award, and the IEEE GRSS Highest Impact Paper Award in 2013. He was granted the IEEE Third Millennium Medal in 2000. He was an Editor of the IEEE TGRS from 2003 to 2008. He has been serving as an Associate Editor of TGRS since 1999, the IEEE GEOSCIENCE AND REMOTE SENSING LETTERS since 2003, and IEEE ACCESS since 2013. He was the Chairman of the Steering Committee of the IEEE JOURNAL OF SELECTED TOPICS IN APPLIED EARTH OBSERVATIONS AND REMOTE SENSING from 2007 to 2010. He is on the International Editorial Board of the *International Journal of Image and Data Fusion*.